

Enhanced Non-linear Response by Manipulating the Dirac Point in the (111) LaTiO₃/SrTiO₃ Interface

G. Tuvia,¹ A. Burshtein,¹ I. Silber,¹ A. Aharony,¹ O. Entin-Wohlman,¹ M. Goldstein,¹ and Y. Dagan^{1,*}

¹*School of Physics and Astronomy, Tel-Aviv University, Tel Aviv, 6997801, Israel*

(Dated: September 15, 2023)

Tunable spin-orbit interaction (SOI) is an important feature for future spin-based devices. In the presence of a magnetic field, SOI induces an asymmetry in the energy bands, which can produce non-linear transport effects ($V \sim I^2$). Here, we focus on such effects to study the role of SOI in the (111) LaTiO₃/SrTiO₃ interface. This system is a convenient platform for understanding the role of SOI since it exhibits a single-band Hall-response through the entire gate-voltage range studied. We report a pronounced rise in the non-linear resistance at a critical in-plane field H_{cr} . This rise disappears with a small out-of-plane field. We explain these results by considering the location of the Dirac point formed at the crossing of the spin-split energy bands. An in-plane magnetic field pushes this point outside of the Fermi surface, and consequently changes the symmetry of the Fermi contours and intensifies the non-linear transport. An out-of-plane magnetic field opens a gap at the Dirac point, thereby significantly diminishing the non-linear effects. We propose that magnetoresistance effects previously reported in interfaces with SOI could be comprehended within our suggested scenario.

Rashba-type spin-orbit interaction (SOI) [1] arises in systems lacking inversion symmetry, such as polar semiconductors [2, 3] and interfaces or surfaces [4, 5]. This interaction lifts the spin degeneracy, leading to the splitting the electronic bands depending on their spin. Such spin-split systems exhibit a multitude of phenomena that hold great promise for spin-based devices [6]. Two-dimensional electron systems are especially interesting in this respect, as the magnitude of their spin-orbit interaction can be tuned by gating [7]. For example, in SrTiO₃ based interfaces, SOI plays a role in phenomena such as weak anti-localization [8], magnetoresistance effects [9], superconductivity [10], and formation of Berry curvature dipoles [11], all of which can be tuned by gate. The (111) surface of SrTiO₃ is particularly intriguing due to its triangular structure, which further reduces the symmetry, leading to rich spin textures [11, 12], and anisotropic magnetoresistance [13].

A useful approach to unravel the effect of SOI is through the measurement of non-linear transport effects ($V \sim I^2$). Under a magnetic field, the spin-split electronic bands become asymmetric, moving in momentum space perpendicular to the magnetic field and the direction in which inversion is broken [3]. This asymmetric band structure can lead to a resistance component which is antisymmetric in both current and magnetic field. While other exotic effects [14, 15] may also manifest in such a behavior, most standard transport effects are symmetric with current and magnetic field. In that sense, the nonlinear response is a cleaner probe for SOI effects.

At the interface between the Mott insulator LaTiO₃ and the band insulator SrTiO₃, the Ti⁺³ and Ti⁺⁴ valences hybridize [16, 17]. For the (001) interface, this

region of hybridized Ti valences was shown to result in two-dimensional conductivity [16] and even superconductivity [18].

Here, we study for the first time the electronic properties of the (111) LaTiO₃/SrTiO₃ interface. We begin by showing that the Hall effect exhibits a perfectly linear one-band-type behavior for all gate voltages studied in this work, up to the highest measured magnetic field of 14 T (Fig. 1(a)). At low temperatures, the interface becomes superconducting (Fig. 1(b)). We find that as the gate-voltage *increases* (higher carrier density and lower sheet resistance), the superconducting transition temperature T_c *decreases*, typical of an “overdoped” regime. Throughout this work, results are plotted as a

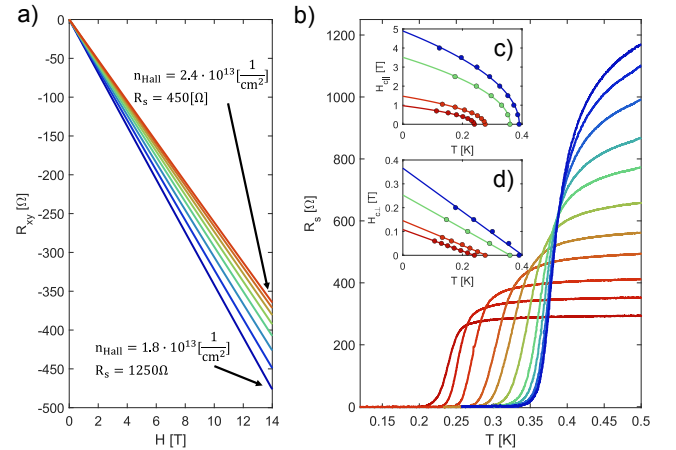


FIG. 1. Hall and superconductivity measurements. (a) Hall effect for various gate-voltages at 10 K, displaying a perfectly linear one-band behavior. (b) Superconducting transitions for various gates-voltages. (c)-(d) In-plane and out-of-plane superconducting critical fields at various temperatures and gates exhibiting a two-dimensional behavior.

* Corresponding author: yodagan@taux.tau.ac.il

function of the sheet resistance instead of gate-voltage to account for the dependence of the resistance on the training history of the gate-voltage (see correspondence between the sheet resistance and the carrier density in Fig. S6 [19]).

To demonstrate the two-dimensional nature of superconductivity, we present the in-plane and out-of-plane superconducting critical magnetic fields in Fig. 1(c)-(d), respectively, for various gate-voltages and temperatures. For all gate-voltages studied here, we observe a linear relation between the out-of-plane superconducting critical field and the temperature, and a square root relation between the in-plane superconducting critical field and temperature. These results support the two-dimensional nature of the superconductivity at the interface. This conclusion is further confirmed by extracting the superconducting coherence length ($\xi = 30 - 55$ nm, depending on gate) and the upper bound for the thickness of the superconducting layer ($d = 8 - 21$ nm), which satisfy $\xi > d$ for all gate-voltages.

To measure the non-linear transport, we apply an alternating current and measure the second harmonic voltage drop as studied elsewhere [3, 12, 20]. To focus on terms which are antisymmetric with magnetic field, the non-linear transport signal is antisymmetrized with respect to the magnetic field. It is useful to define $\gamma = \frac{2R_{2\omega}}{R_0HI}$, where $R_{2\omega} = V_{2\omega}/I$ is the second-harmonic resistance, R_0 is the Ohmic resistance, H is the magnetic field, I is the current, γ is the coefficient of the nonlinear term in the resistance:

$$R(I, H) = R_0(1 + \beta H^2 + \gamma IH), \quad (1)$$

and β is the orbital magnetoresistance coefficient.

The second-harmonic resistance of the interface exhibits a pronounced enhancement beyond a critical transverse magnetic field H_{cr} (Fig. 2; “transverse” denotes an in-plane magnetic field applied perpendicular to the current). For the low-field regime ($H < H_{cr}$), the second-harmonic effect is small and depends linearly on the transverse magnetic field. This behavior is further illustrated in the low-field inset, where γ has a sinusoidal dependence on the in-plane angle ϕ , defined as the angle between the in-plane magnetic field and the current (bottom inset). However, as the magnetic field exceeds the critical magnetic field ($H > H_{cr}$), γ increases substantially and exhibits oscillations depending on ϕ (see high-field inset). As can be seen in the supplemental material Fig. S2 [19], these high-field oscillations depend on the magnitude of the magnetic field and on direction of the current with respect to the crystal axes.

The sharp increase of $R_{2\omega}$ shown in Fig. 2 is extremely sensitive to the application of an out-of-plane magnetic field. This can be seen in Fig. 3(a), where a magnetic field of 9 T ($> H_{cr}$) is rotated out of the plane of the interface, perpendicular to the current (see top image in Fig. 3(e) for clarity). γ rapidly decays with the introduction of a small out-of-plane contribution. Conversely,

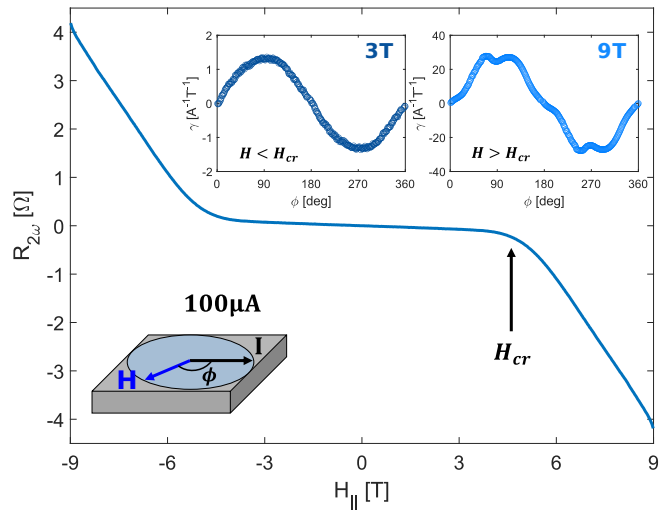


FIG. 2. The second-harmonic resistance versus the in-plane magnetic field at $T=3$ K and $R_s=380$ Ω ; H_{cr} is indicated. Inset: Dependence of $\gamma = \frac{2R_{2\omega}}{R_0HI}$ on the in-plane angle ϕ . In the low-field regime, the effect depends only on the component of the field perpendicular to the current. In the high-field regime, the effect also depends on the in-plane field angle ϕ .

Fig. 3(b) shows the low-field behavior ($H < H_{cr}$), where γ is much smaller, and depends linearly on the in-plane magnetic field component.

To further investigate the influence of out-of-plane magnetic fields, a constant in-plane field of 7.8 T ($> H_{cr}$) was rotated while applying various out-of-plane fields (see bottom panel of Fig. 3(e)). Fig. 3(c) presents the results for out-of-plane fields of +4.5 T (red), -4.5 T (black), and 0 T (blue). Although $H > H_{cr}$ in these measurements, the signal with an out-of-plane contribution resembles the behavior observed in the low-field regime, suggesting that an out-of-plane magnetic field mostly counteracts the high field enhancement of γ .

The same magnetic field measurement scheme used in Fig. 3(c) was employed while measuring the first-harmonic sheet resistance R_s (see Fig. 3(d)). The measurements performed with no out-of-plane field (blue curve) primarily exhibit a two-fold effect as a function of ϕ , accompanied by four-fold and six-fold contributions (see Fig. S3 [19]), similar to those previously reported for the (111) $\text{LaAlO}_3/\text{SrTiO}_3$ interface [13]. However, upon the introduction of an out-of-plane magnetic field (red/black curves), an unusual anisotropy emerges. This anisotropic component breaks the mirror symmetry of the magnetic field with respect to the interface, $R(H_{||}, H_{\perp}) \neq R(H_{||}, -H_{\perp})$. Interestingly, for a particular in-plane angle, this mirror symmetry is preserved. This angle (defined as ϕ_0) exhibits a three-fold dependence on the crystal axis along which current is driven (as seen in Fig. S4 [19]). While the understanding of this effect lies beyond the scope of this work, its three-fold nature and dependence on the out-of-plane magnetic field suggests that it is a consequence of the three-fold out-of-

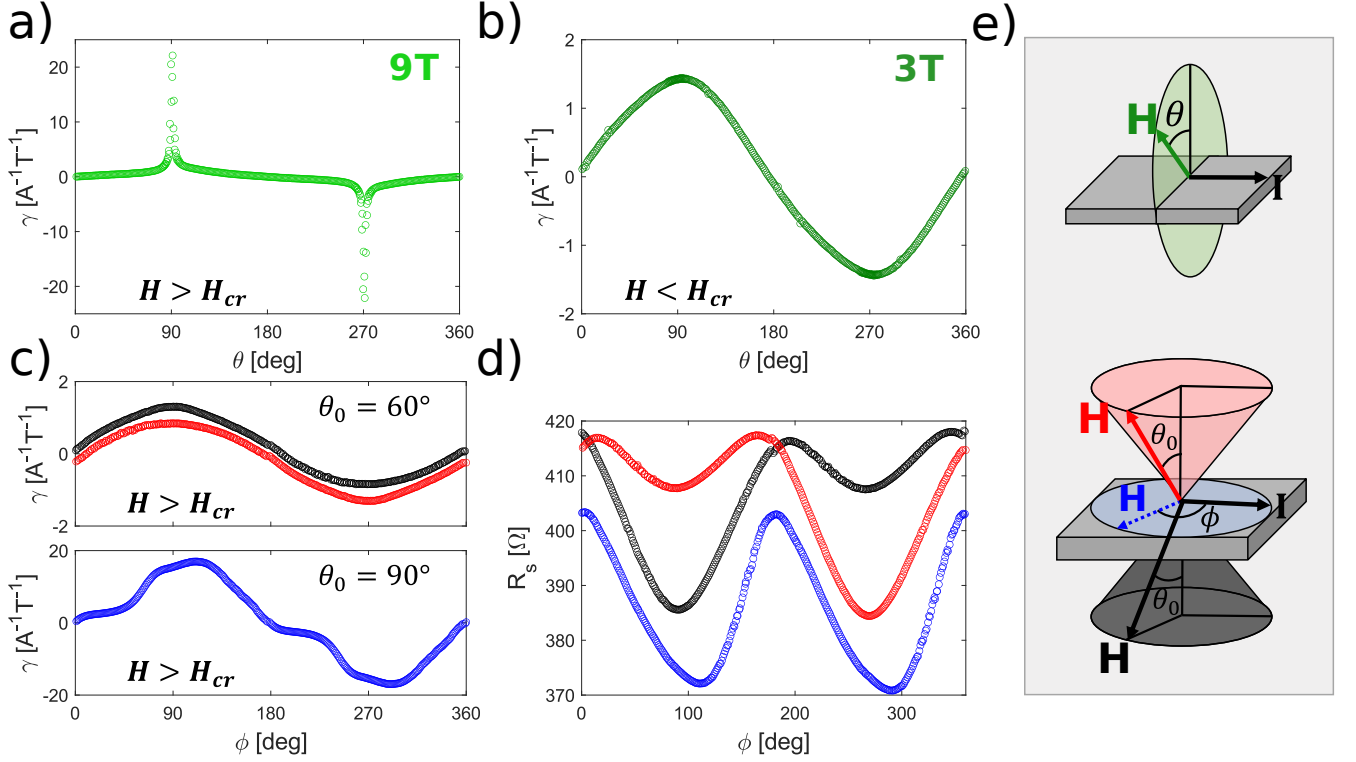


FIG. 3. Effects of the out-of-plane magnetic field. (a,b) γ is shown as a function of the out-of-plane magnetic field angle θ for total field magnitudes of 9 T (a) and 3 T (b). A sharp increase in γ is observed for the high field regime when the magnetic field is in-plane. (c) γ is shown versus the in-plane angle ϕ for $H_{\parallel} = 7.8$ T and $H_{\perp} = 4.5$ T (red), -4.5 T (black), and 0 T (blue). (d) Similar magnetic field scheme like (c) for the first-harmonic measurements. Note the mirror symmetry breaking for the red and black curves. (e) Sketch of the magnetic field configurations employed in the measurements presented in this figure. Temperatures and sheet resistances for these figures slightly vary due to different cool-downs: (a) $T = 3$ K and $R_s = 380$ Ω , (b) $T = 1.8$ K and $R_s = 412$ Ω , (c)-(d) $T = 1.9$ K and $R_s = 407$ Ω .

plane tilt of the spin texture observed for the surface of (111) SrTiO₃ [12].

The high-field enhancement of $R_{2\omega}$ decays with temperature, almost vanishing at ≈ 10 K. This behavior can be observed in Fig. 4(a), where a transverse magnetic field is applied at various temperatures. To quantify the effect of temperature, the γ factor at 9 T is plotted in Fig. 4(b) for various temperatures after subtracting the small low-field contribution, extrapolated to 9 T (the result is defined as $\Delta\gamma$). As shown in Fig. S5 (b) [19], the critical field H_{cr} does not change within this temperature range. A similar analysis was performed as a function of gate-voltage and is shown in Fig. 4(c)-(d). A strong decay of the effect is observed as the gate-voltage becomes more negative. In contrast to the effect of temperature, the critical field H_{cr} changes with the gate-voltage (see Fig. S5 (a) [19]), reflecting a change of the chemical potential and the SOI magnitude.

To elucidate the critical behavior observed in the second-harmonic transport, we propose a minimal model that can capture the essential features observed in experiment. Our model assumes a two-dimensional electron system with a simple parabolic dispersion and a Rashba-

type spin-orbit interaction in the presence of a Zeeman magnetic field:

$$\mathcal{H} = \frac{k^2}{2m} + \lambda(k_x\sigma_y - k_y\sigma_x) - B_y\sigma_y - B_z\sigma_z, \quad (2)$$

where λ represents the magnitude of the SOI, $k_{x/y}$ denote the momentum components which are parallel/perpendicular to the current, $\sigma_{x/y/z}$ are the Pauli matrices, and B_y/B_z are the transverse/out-of-plane magnetic field components. Note that throughout this work, B is used for magnetic fields in the calculations in units of energy assuming $g=2$, while H is used for the magnetic fields applied in the experiment.

Previous calculations by Ideue *et al.* [3] have shown that for such a system, the geometry of the Fermi surface changes at critical values of the magnetic field or chemical potential, leading to a change in γ . To map this scenario onto the (111) LaTiO₃/SrTiO₃ interface studied here, we estimate the relevant parameters of the system. The spin-orbit energy of SrTiO₃ based interfaces is estimated at a few meV [9–11] while the electron density of a few 10^{13} [$\frac{1}{\text{cm}^2}$] results in a chemical potential of roughly 100meV. To ensure that the estimation of the spin-orbit

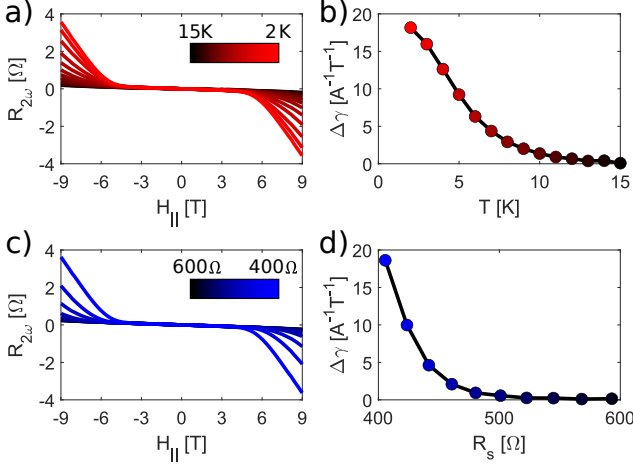


FIG. 4. (a) Second-harmonic resistance versus transverse magnetic field at different temperatures. (b) γ at 9 T after subtracting the low-field contribution, versus temperature. (c,d) Similar to (a,b) but as a function of gate-voltage represented by the sheet resistance (R_s). The effect quickly decays at more negative gates-voltages (higher resistances). Temperature-dependent measurements were conducted for the lowest R_s , gate-dependent measurements were conducted at 2 K.

energy is reasonable, we perform standard magnetoresistance measurements at low temperatures (Fig. S6 [19]). The relatively small spin-splitting effect means that, for $B = 0$, the spin-split energy bands cross at a single Dirac point, below the Fermi energy. Once a transverse magnetic field B_y is applied, the energy of the Dirac point increases, reaching the Fermi energy at the critical field $B_{cr} = \sqrt{2m\lambda^2\mu}$. Within the relevant parameter regime, the calculated B_{cr} falls reasonably close to the critical field observed in experiment.

As we now show, the exclusion of the Dirac point from the Fermi surface leads to a dramatic increase in $R_{2\omega}$, similar to our experimental observation. The second-harmonic resistance is proportional to σ_2/σ_1^2 , where $J^{(i)} = \sigma_i E^i$. By expanding the Boltzmann equation to a second order in the electric field within the single relaxation time approximation [19], we obtain the second order current:

$$J^{(2)} = -e^3 \tau^2 E^2 \sum_{r=\pm} \int \frac{dk_x dk_y}{(2\pi)^2} \frac{\partial^3 \varepsilon_k^r}{\partial k_x^3} f_0^r, \quad (3)$$

where τ is the scattering time, E is the electric field applied in the \hat{x} direction, f_0^\pm are the Fermi-Dirac distributions of the bands, and ε_k^r are the corresponding energies. Considering first the case of $B_z = 0$, the energy bands are given by:

$$\varepsilon_k^\pm = \frac{k^2}{2m} \pm \sqrt{(\lambda k_x - B_y)^2 + \lambda^2 k_y^2}. \quad (4)$$

While the third derivative of the parabolic term $k^2/2m$ in Eq. (4) vanishes, the Dirac point acts as a source for

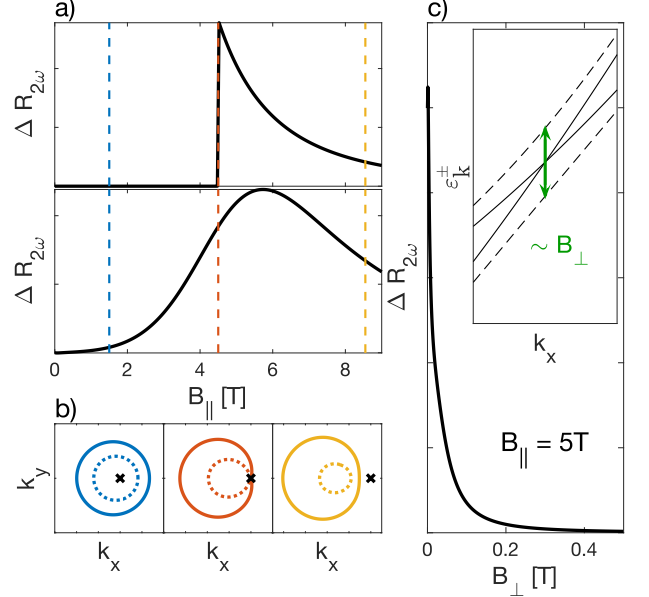


FIG. 5. Minimal model calculations. (a) Calculated second-harmonic resistance as function of transverse magnetic field with no out-of-plane field (top panel) and a small out-of-plane field (bottom panel). (b) Fermi contours for $B_{\parallel} < B_{cr}$, $B_{\parallel} = B_{cr}$, $B_{\parallel} > B_{cr}$. For every scenario, the location of the Dirac point is marked. (c) Second-harmonic resistance vs. the perpendicular magnetic field with constant high transverse magnetic field. Inset: Illustration of band gap opening with perpendicular magnetic field.

higher derivatives, and yields a non-vanishing contribution to the integrands in Eq. (3). In section 1 of the supplemental material [19] we show that for $B_y < B_{cr}$, the sum of third derivatives of the bands is antisymmetric under a π rotation around the Dirac point, such that $J^{(2)} = 0$. This symmetry is broken for $B_y > B_{cr}$, where the Dirac point is excluded from both Fermi surfaces, and $J^{(2)}$ assumes a finite value. Utilizing the above expressions, we calculate $R_{2\omega}$ as function of B_y . The result, presented in the top panel of Fig. 5(a), shows that the second harmonic signal is zero for low fields ($B_y < B_{cr}$), significantly increases once the Fermi contours intersect at $B_y = B_{cr}$, and finally decreases for $B_y > B_{cr}$. The position of this Dirac point with respect to the Fermi contours is illustrated in Fig. 5(b) for several values of the transverse magnetic field. We note that the spin-texture of the Fermi contours also changes at the critical field — for the low-field regime, the spin texture completes a 2π rotation when going along the Fermi contours while it does not above the critical field [19]. While this Dirac point mechanism can explain the critical magnetic field observed in experiment, the strong decay of γ with temperature and gate-voltage shown in Fig. 4(b), (d) requires an analysis beyond the single relaxation time approximation used here [19].

The presence of an energy gap between the spin-split

bands can significantly change the ideal result presented in Fig. 5(a) (top panel). In the bottom panel of Fig. 5(a), we show the calculated $R_{2\omega}$ as a function of the transverse magnetic field B_y when a small gap is opened by a perpendicular magnetic field, equivalent to $B_z = 10$ mT. This gap adds a new asymmetry to the energy bands, leading to a small non-zero coefficient below the critical field and a much more gradual increase of $R_{2\omega}$ at the critical field. In Fig. 5(c), we show the calculated $R_{2\omega}$ in a constant transverse magnetic field ($B_y > B_{cr}$) while a perpendicular magnetic field B_z is applied. The second-harmonic signal quickly decays, similar to the experimental result shown in Fig. 3. This decay reflects the fact that the gap smooths the Dirac point, as seen in Fig. 5(c), which substantially decreases the magnitude of the third derivative.

It is interesting to compare the (111) LaTiO₃/SrTiO₃ interface studied here to the more extensively studied LaAlO₃/SrTiO₃ interface. While for both (001) and (111) LaAlO₃/SrTiO₃ interfaces, the overdoped regime of superconductivity is accompanied by a two-band Hall signal [21–23], here the overdoped regime is observed with a single band Hall effect (Fig. 1). Likewise, several magneto-transport effects, such as the in-plane-magnetic-field-induced anomalous Hall effect [9, 24], and anisotropic magnetoresistance [13, 24], are observed in LaAlO₃/SrTiO₃ interfaces only once a two-band Hall behavior is also observed. However, for the interface studied here, they appear with only a single occupied energy band (see Fig. S8 and S3 for anomalous Hall and magnetoresistance measurements, respectively [19]). Moreover, these effects are strongest at low-temperatures, high gate-voltages, and when a strong in-plane magnetic field is applied, which are exactly the conditions where γ is large. As noted in previous works [21–23], the Rashba SOI only adds a small correction to the band structure. However, as we show in this work, the manipulation of the spin-orbit induced Dirac point changes the symmetry of the energy bands, which has a substantial effect on the non-linear transport, and possibly also the linear

magneto-transport.

In summary, we measure the new (111) LaTiO₃/SrTiO₃ interface. We observe superconductivity in this interface along with one-band-type Hall-signal. This behavior is observed even when T_c is decreased when adding charge carriers (overdoped regime), in contrast to the well studied LaAlO₃/SrTiO₃ interfaces. Our main finding is a sharp increase of the magnitude of the non-linear transport of the (111) LaTiO₃/SrTiO₃ interface at a critical magnetic field H_{cr} . By employing a minimal model incorporating spin-orbit interaction at a generic interface, we show that H_{cr} can be understood as the field in which the spin-orbit-induced Dirac point is excluded from the Fermi surface. According to our model, beyond this field, the symmetry and the spin-texture of the Fermi contours change simultaneously. We further show that a minuscule out-of-plane magnetic field opens a gap between the spin-split bands, which significantly reduces the second-harmonic effect, as observed in experiment. We suggest that this mechanism sheds light on some of the unusual magneto-transport effects observed in previous experiments.

Acknowledgements

We thank Tobias Holder, Roni Ilan, and Shay Sandik for useful discussions. Asaf Yagoda and Elad Mileikowsky assisted with the transport setup. This work was partially supported (Y.D.) By the Israeli Science Foundation under grant 476/22 and by the PAZI foundation under grant 326-1/20. M.G. was supported by the Israel Science Foundation (ISF) and the Directorate for Defense Research and Development (DDR&D) Grant No. 3427/21, and by the US-Israel Binational Science Foundation (BSF) Grant No. 2020072. A.B. is supported by the Adams Fellowship Program of the Israel Academy of Sciences and Humanities.

-
- [1] E. Rashba, *Sov. Phys.-Solid State* **2**, 1109 (1960).
 - [2] K. Ishizaka, M. S. Bahramy, H. Murakawa, M. Sakano, T. Shimojima, T. Sonobe, K. Koizumi, S. Shin, H. Miyahara, A. Kimura, K. Miyamoto, T. Okuda, H. Namatame, M. Taniguchi, R. Arita, N. Nagaosa, K. Kobayashi, Y. Murakami, R. Kumai, Y. Kaneko, Y. Onose, and Y. Tokura, *Nature Materials* **10**, 521 (2011).
 - [3] T. Ideue, K. Hamamoto, S. Koshikawa, M. Ezawa, S. Shimizu, Y. Kaneko, Y. Tokura, N. Nagaosa, and Y. Iwasa, *Nature Physics* **13**, 578 (2017).
 - [4] A. F. Santander-Syro, F. Fortuna, C. Bareille, T. C. Rödel, G. Landolt, N. C. Plumb, J. H. Dil, and M. Radović, *Nature Materials* **13**, 1085 (2014).
 - [5] S. LaShell, B. A. McDougall, and E. Jensen, *Phys. Rev. Lett.* **77**, 3419 (1996).
 - [6] A. Manchon, H. C. Koo, J. Nitta, S. M. Frolov, and R. A. Duine, *Nature Materials* **14**, 871 (2015).
 - [7] K. Premasiri and X. P. Gao, *Journal of Physics: Condensed Matter* **31**, 193001 (2019).
 - [8] D. Rakhmilevitch, M. Ben Shalom, M. Eshkol, A. Tsukernik, A. Palevski, and Y. Dagan, *Phys. Rev. B* **82**, 235119 (2010).
 - [9] M. Ben Shalom, M. Sachs, D. Rakhmilevitch, A. Palevski, and Y. Dagan, *Phys. Rev. Lett.* **104**, 126802 (2010).
 - [10] P. K. Rout, E. Maniv, and Y. Dagan, *Phys. Rev. Lett.* **119**, 237002 (2017).
 - [11] E. Lesne, Y. G. Sağlam, R. Battilomo, M. T. Mercaldo, T. C. van Thiel, U. Filippozzi, C. Noce, M. Cuoco, G. A. Steele, C. Ortix, and A. D. Caviglia, *Nature Materials* **22**, 576 (2023).

- [12] P. He, S. M. Walker, S. S.-L. Zhang, F. Y. Bruno, M. S. Bahramy, J. M. Lee, R. Ramaswamy, K. Cai, O. Heinonen, G. Vignale, F. Baumberger, and H. Yang, *Phys. Rev. Lett.* **120**, 266802 (2018).
- [13] P. K. Rout, I. Agireen, E. Maniv, M. Goldstein, and Y. Dagan, *Phys. Rev. B* **95**, 241107 (2017).
- [14] G. L. J. A. Rikken and P. Wyder, *Phys. Rev. Lett.* **94**, 016601 (2005).
- [15] C. O. Avci, K. Garello, A. Ghosh, M. Gabureac, S. F. Alvarado, and P. Gambardella, *Nature Physics* **11**, 570 (2015).
- [16] A. Ohtomo, D. A. Muller, J. L. Grazul, and H. Y. Hwang, *Nature* **419**, 378 (2002).
- [17] Y. Wang, Y. Liang, M. Meng, Q. An, B. Ge, M. Liu, F. Yang, and J. Guo, *Journal of Applied Physics* **128**, 035301 (2020).
- [18] J. Biscaras, N. Bergeal, A. Kushwaha, T. Wolf, A. Rastogi, R. C. Budhani, and J. Lesueur, *Nature Communications* **1**, 89 (2010).
- [19] See Supplemental Material for details.
- [20] D. Choe, M.-J. Jin, S.-I. Kim, H.-J. Choi, J. Jo, I. Oh, J. Park, H. Jin, H. C. Koo, B.-C. Min, S. Hong, H.-W. Lee, S.-H. Baek, and J.-W. Yoo, *Nature Communications* **10**, 4510 (2019).
- [21] A. Joshua, S. Pecker, J. Ruhman, E. Altman, and S. Ilani, *Nature Communications* **3**, 1129 (2012).
- [22] E. Maniv, M. B. Shalom, A. Ron, M. Mograbi, A. Palevski, M. Goldstein, and Y. Dagan, *Nature Communications* **6**, 8239 (2015).
- [23] U. Khanna, P. K. Rout, M. Mograbi, G. Tuvia, I. Leermakers, U. Zeitler, Y. Dagan, and M. Goldstein, *Phys. Rev. Lett.* **123**, 036805 (2019).
- [24] A. Joshua, J. Ruhman, S. Pecker, E. Altman, and S. Ilani, *Proceedings of the National Academy of Sciences* **110**, 9633 (2013).

Supplementary - Enhanced Non-linear Response by Manipulating the Dirac Point in the (111) $\text{LaTiO}_3/\text{SrTiO}_3$ Interface

G. Tuvia,¹ A. Burshtein,¹ I. Silber,¹ A. Aharony,¹ O. Entin-Wohlman,¹ M. Goldstein,¹ and Y. Dagan^{1,*}

¹*School of Physics and Astronomy, Tel-Aviv University, Tel Aviv, 6997801, Israel*

(Dated: September 15, 2023)

arXiv:2309.07706v1 [cond-mat.str-el] 14 Sep 2023

* Corresponding author: yodagan@tauex.tau.ac.il

I. SUPPLEMENTARY SECTION 1 — BOLTZMANN-EQUATION CALCULATIONS

A. Hamiltonian and energy bands

We consider a 2D Hamiltonian with a parabolic dispersion relation, an external magnetic field, and a Rashba spin-orbit interaction term,

$$\mathcal{H} = \frac{k^2}{2m} + \lambda(k_x\sigma_y - k_y\sigma_x) - B_x\sigma_x - B_y\sigma_y - B_z\sigma_z, \quad (\text{S1})$$

where $k_{x,y}$ denote the momentum components, λ is the spin-orbit coupling coefficient (in momentum units), $B_{x,y,z}$ are the components of the magnetic field (in energy units), $\sigma_{x,y,z}$ are the Pauli matrices, and m is the effective mass of the electrons. Here we consider only the Zeeman field and neglect the orbital effect of the magnetic field. The energy bands are given by

$$\varepsilon^\pm(k) = \frac{k^2}{2m} \pm \sqrt{(\lambda k_x - B_y)^2 + (\lambda k_y + B_x)^2 + B_z^2}. \quad (\text{S2})$$

It is more convenient to redefine the momentum as $p_x = k_x - \frac{B_y}{\lambda}$ and $p_y = k_y + \frac{B_x}{\lambda}$, so that the minimum distance between the bands is at the origin, $p = 0$ (where $p^2 = p_x^2 + p_y^2$):

$$\varepsilon^\pm(p) = \frac{p^2}{2m} - \frac{pB_\parallel \sin(\theta - \varphi)}{m\lambda} + \frac{B_\parallel^2}{2m\lambda^2} \pm \sqrt{\lambda^2 p^2 + B_z^2}, \quad (\text{S3})$$

where $B_x = B_\parallel \cos \varphi$, $B_y = B_\parallel \sin \varphi$ are the components of the in-plane magnetic field, and $p_x = p \cos \theta$, $p_y = p \sin \theta$ are the components of the momentum. In the absence of an out-of-plane magnetic field, the bands intersect at the origin; a gap is opened for $B_z \neq 0$. The corresponding eigenvectors are spin-polarized,

$$\psi^\pm(\theta) = \frac{1}{\sqrt{2}} \begin{pmatrix} 1 \\ \pm i \text{sign}(\lambda) e^{i\theta} \end{pmatrix}. \quad (\text{S4})$$

The Fermi momenta $p_\pm^\pm(\theta)$ are the solutions to $\mu = \varepsilon^\pm(p_\pm^\pm(\theta))$, where μ is the chemical potential. At $B_z = 0$, an analytical solution is obtained,

$$p_r^\pm(\theta) = \frac{B_\parallel}{\lambda} \sin(\theta - \varphi) - r |\lambda| m \pm \sqrt{2m\tilde{\mu} - \frac{B_\parallel^2}{\lambda^2} \cos^2(\theta - \varphi) - 2r \text{sign}(\lambda) m B_\parallel \sin(\theta - \varphi)}, \quad (\text{S5})$$

where $r = \pm$ labels the bands, and $\tilde{\mu} = \mu + m\lambda^2/2$ is the chemical potential measured with respect to the bottom of the lower band at $B_\parallel = 0$. The momenta $p_r^-(\theta)$ and $p_r^+(\theta)$ constitute the inner and outer contours of the Fermi surface of the r band, and are defined only for angles θ for which $p_r^\pm(\theta) \in \mathbb{R}^+$. The critical field, $B_{cr} = \sqrt{2m\lambda^2\mu}$, determines whether or not the origin $p = 0$ is included in the Fermi surface, as demonstrated in Fig. 5 in the main text. Namely, for $B_\parallel < B_{cr}$, one finds that $p_\pm^-(\theta) < 0$ and $p_\pm^+(\theta) \in \mathbb{R}^+$ for any θ , so $p = 0$ is included in the Fermi surface of both bands. For $B_\parallel > B_{cr}$, there are angles where the Fermi momenta are undefined, such that $p = 0$ is excluded from the Fermi surface of the bands. We assume throughout that $m\lambda^2 \ll B_{cr}, \mu$, and also that $B_\parallel \ll \mu$, such that both bands are occupied for the parameters used in the experiment. As mentioned in the main text, typical values of λ and μ in the LaTiO₃/SrTiO₃ interface yield critical fields on the order of a few Tesla, within the experimental range of applied magnetic fields.

B. Calculation of the first and second harmonic currents

We follow the method used in Ref. [1] for calculating the second-harmonic resistance. We begin by writing down the Boltzmann equation for the distribution functions of the bands, $f^\pm(\vec{E}, \mu, \vec{p})$, for an electric field applied in the \hat{x} direction, $\vec{E} = E\hat{x}$. Within the relaxation-time approximation, one finds

$$-e\vec{E} \cdot \vec{\nabla}_p f^\pm = -eE \frac{\partial f^\pm}{\partial p_x} = -\frac{1}{\tau} (f^\pm - f_0^\pm), \quad (\text{S6})$$

where $f_0^\pm = 1 / (\exp \{ (\varepsilon_p^\pm - \mu) / k_B T \} + 1)$ is the Fermi-Dirac distribution function, and τ is the scattering time. Expanding f^\pm as a power series in the electric field E , $f^\pm = f_0^\pm + f_1^\pm + f_2^\pm + \dots$, with $f_n^\pm \sim E^n$, we find

$$-eE \frac{\partial}{\partial p_x} \sum_{n=0}^{\infty} f_n^\pm = -\frac{1}{\tau} \sum_{n=1}^{\infty} f_n^\pm. \quad (\text{S7})$$

Equating the coefficients of the electric field term-by-term yields

$$f_n^\pm = eE\tau \frac{\partial f_{n-1}^\pm}{\partial p_x}. \quad (\text{S8})$$

We may then find the current from the distribution functions. The n -th harmonic contribution to the current is given by

$$\begin{aligned} J^{(n)} &= \sum_{r=\pm} \int \frac{dp_x dp_y}{(2\pi)^2} \left(-e \frac{\partial \varepsilon_p^r}{\partial p_x} \right) f_n^r \\ &= (-1)^{n+1} e (e\tau E)^n \sum_{r=\pm} \int \frac{dp_x dp_y}{(2\pi)^2} \frac{\partial^{n+1} \varepsilon_p^r}{\partial p_x^{n+1}} f_0^r. \end{aligned} \quad (\text{S9})$$

The first and second harmonics are given by

$$\begin{aligned} J^{(1)} &= \frac{e^2 \lambda^2 \tau E}{(2\pi)^2} \int dp d\theta \left(\frac{p}{m\lambda^2} (f_0^+ + f_0^-) + \frac{\lambda^2 p^3 \sin^2 \theta + p B_z^2}{(\lambda^2 p^2 + B_z^2)^{3/2}} (f_0^+ - f_0^-) \right), \\ J^{(2)} &= \frac{3e^3 \lambda^4 \tau^2 E^2}{(2\pi)^2} \int dp d\theta \frac{\lambda^2 p^4 \cos \theta \sin^2 \theta + B_z^2 p^2 \cos \theta}{(\lambda^2 p^2 + B_z^2)^{5/2}} (f_0^+ - f_0^-). \end{aligned} \quad (\text{S10})$$

Note that the dependence on B_{\parallel} is encoded in the Fermi-Dirac distribution functions. The n -th harmonic conductance is defined by $\sigma_n = E^n / J^{(n)}$; the second-harmonic resistance is given by $R_{2\omega} \sim \sigma_2 / \sigma_1^2$, and is independent of the scattering time τ .

The double integrals may be evaluated numerically for any value of B_{\parallel}, B_z at any temperature. To gain analytical insight, consider the case $B_z = 0$ and $T = 0$. The Fermi-Dirac distributions become step functions, and the integrals over p may be easily evaluated analytically. Below the critical field, $B_{\parallel} < B_{cr}$, one finds from Eq. (S5) that $p_r^-(\theta) < 0$ and $p_r^+(\theta) > 0$ for all θ , leading to

$$\begin{aligned} J^{(1)}(B_{\parallel} < B_{cr}) &= \frac{e^2 \tau E}{(2\pi)^2} \int_0^{2\pi} d\theta \left(\frac{(p_+^+(\theta))^2 + (p_-^+(\theta))^2}{2m} + |\lambda| (p_+^+(\theta) - p_-^+(\theta)) \sin^2 \theta \right), \\ J^{(2)}(B_{\parallel} < B_{cr}) &= \frac{3e^3 |\lambda| \tau^2 E^2}{(2\pi)^2} \int_0^{2\pi} d\theta \log \left(\frac{p_+^+(\theta)}{p_-^+(\theta)} \right) \cos \theta \sin^2 \theta. \end{aligned} \quad (\text{S11})$$

Above the critical field, there are angles θ for which the Fermi momenta are either imaginary or negative. The p integrals may be evaluated as before, but the θ integral is restricted to angles for which $p_{\pm}^{\pm}(\theta) \in \mathbb{R}^+$:

$$\begin{aligned} J^{(1)}(B_{\parallel} > B_{cr}) &= \frac{e^2 \tau E}{(2\pi)^2} \int_{p_{\pm}^{\pm}(\theta) \in \mathbb{R}^+} d\theta \\ &\times \left(\frac{(p_+^+(\theta))^2 + (p_-^+(\theta))^2 - (p_+^-(\theta))^2 - (p_-^-(\theta))^2}{2m} + |\lambda| (p_-^+(\theta) - p_+^+(\theta) + p_+^-(\theta) - p_-^-(\theta)) \sin^2 \theta \right), \\ J^{(2)}(B_{\parallel} > B_{cr}) &= \frac{3e^3 |\lambda| \tau^2 E^2}{(2\pi)^2} \int_{p_{\pm}^{\pm}(\theta) \in \mathbb{R}^+} d\theta \log \left(\frac{p_+^+(\theta) p_-^-(\theta)}{p_-^+(\theta) p_+^-(\theta)} \right) \cos \theta \sin^2 \theta. \end{aligned} \quad (\text{S12})$$

For the first harmonic current, one finds $J^{(1)} = e^2 \tau m / \pi \times (m\lambda^2 + \mu)$ at any $B_{\parallel} < B_y$, and a very small and continuous deviation from this value at $B_{\parallel} > B_y$. Next, consider the integrand of $J^{(2)}$. Using Eq. (S5), we find that the ratio $p_+^{\xi}(\theta) / p_-^{\xi}(\theta)$, for both $\xi = \pm$, is symmetric under the transformation $\theta \rightarrow \theta + \pi$ [1], implying that the integrand of

$J^{(2)}$ above is antisymmetric under such a transformation. Hence, if the origin is included in Fermi surface, so that the integral of $J^{(2)}$ runs over $0 \leq \theta < 2\pi$, one finds $J^{(2)} = 0$. If, however, $B_{\parallel} > B_{cr}$, such that the origin is excluded from the Fermi surface, the integral of $J^{(2)}$ is restricted to a smaller subset of angles θ ; in particular, there are angles θ that are included in the integration regime for which $\theta + \pi$ is excluded from the integral. Hence, above the critical field, the second harmonic current no longer vanishes. At the critical field, $B_{\parallel} = B_{cr}$, the derivative of ε_p^{\pm} with respect to p_x is not continuous; this explains the jump in the second harmonic current, which is determined by the third-order derivative $\partial^3 \varepsilon_p^{\pm} / \partial p_x^3$ [see Eq. (S9)].

As B_{\parallel} is increased beyond the critical field, we expect $J^{(2)}$ to decrease. Let us show this for $B_x = 0$ ($\varphi = \pi/2$). Expanding the logarithm in the $J^{(2)}$ integral in Eq. (S12) for $B_{\parallel} = B_y \gg B_{cr}$, one finds

$$\log \left(\frac{p_+^+(\theta) p_-^-(\theta)}{p_-^+(\theta) p_+^-(\theta)} \right) \approx \frac{4m\lambda^2}{B_y^2} \sqrt{2m\lambda^2 \tilde{\mu} - B_y^2 \sin^2 \theta}. \quad (\text{S13})$$

Plugging into the integral yields

$$\begin{aligned} J^{(2)}(B_y \gg B_{cr}) &\approx \frac{3|\lambda| e^3 \tau^2 E^2}{(2\pi)^2} \frac{4m\lambda^2}{B_y^2} \int_{\sin^2 \theta < \frac{2m\lambda^2 \tilde{\mu}}{B_y^2}, \frac{B_y}{\lambda} \cos \theta < 0} d\theta \sin^2 \theta \cos \theta \sqrt{2m\lambda^2 \tilde{\mu} - B_y^2 \sin^2 \theta} \\ &= \frac{3\pi |\lambda| e^3 \tau^2 E^2}{2(2\pi)^2} \frac{m\lambda^2}{B_y} \left(\frac{B_{cr}}{B_y} \right)^2. \end{aligned} \quad (\text{S14})$$

This shows that the second-harmonic current decreases as B_{\parallel} is increased far beyond the critical field.

C. Perpendicular magnetic field and the role of a gap

The presence of an out-of-plane field B_z introduces two major differences. First, the antisymmetry of the integrand in Eq. (S10) is broken, so that $J^{(2)} \neq 0$ also for $B_{\parallel} < B_{cr}$. Second, B_z opens a gap (as demonstrated in Figure 5 of the main text), so that the derivatives of the dispersion relation with respect to p_x become continuous, leading to the suppression of the jump at $B_{\parallel} = B_{cr}$. We stress that such features should be generic; there are many different terms that could be added to the Hamiltonian which would break the antisymmetry of the $J^{(2)}$ integrand or open a gap and suppress the jump at $B_{\parallel} = B_{cr}$. We demonstrate this point by adding a cubic ‘‘warping’’ spin-orbit term to the Hamiltonian in Eq. (S1):

$$\mathcal{H}_{\zeta} = \frac{\zeta}{2} (k_+^3 + k_-^3) \sigma_z, \quad (\text{S15})$$

with $k_{\pm} = k_x \pm ik_y$. The energy bands are readily given by

$$\varepsilon_p^{\pm} = \frac{p^2}{2m} - \frac{pB_{\parallel} \sin(\theta - \varphi)}{m\lambda} + \frac{B_{\parallel}^2}{2m\lambda^2} \pm \sqrt{\lambda^2 p^2 + \left(\zeta \left(p \cos \theta + \frac{B_y}{\lambda} \right) \left[\left(p \cos \theta + \frac{B_y}{\lambda} \right)^2 - 3 \left(p \sin \theta - \frac{B_x}{\lambda} \right)^2 \right] - B_z \right)^2}. \quad (\text{S16})$$

Note that, even in the absence of an out-of-plane field B_z , a gap opens if $\zeta \neq 0$, and the bands do not intersect at $p = 0$. The double integrals in Eq. (S9) may be evaluated numerically, revealing a linear growth of $J^{(2)}$ in B_y for $B_y \ll B_{cr}$.

D. Berry curvature and spin texture

The Hamiltonian in Eq. (S1) may be written as $\mathcal{H} = k^2/2m + \mathbf{d} \cdot \boldsymbol{\sigma}$, with $\mathbf{d} = (-\lambda k_y - B_x, \lambda k_x - B_y, -B_z)$. The crossing point at $(k_x, k_y) = (B_y/\lambda, -B_x/\lambda)$ ($p = 0$) is a Dirac point, whose corresponding Dirac cone is titled by the parabolic dispersion relation, as demonstrated in Figure S1. Its associated Berry curvature is given by $\Omega^{\pm} = \pm \hat{\mathbf{d}} \cdot (\partial_{k_x} \hat{\mathbf{d}} \times \partial_{k_y} \hat{\mathbf{d}}) / 2 = \pm \lambda^2 B_z / |\mathbf{d}|^3$, where + and – correspond to the two energy bands. In the limit of vanishing perpendicular field B_z , the curvature is given by a delta function at the p origin, $\Omega^{\pm} = \pm \pi \delta^{(2)}(p)$. When the in-plane magnetic field is below the critical field, $B_{\parallel} < B_{cr}$, the Dirac point is enclosed by the Fermi contours of both

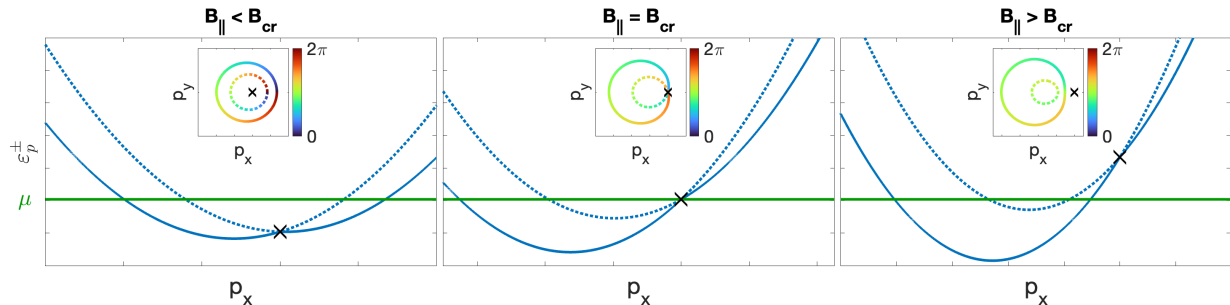


FIG. S1. Energy bands ε_p^- and ε_p^+ , plotted in solid and dotted lines, respectively, as a function of p_x and at $p_y = 0$, for transverse magnetic fields below, at, and above the critical field. The Dirac point at $p = 0$ is marked by an “x” in all figures. The insets show the angle of the spins along the Fermi contours; the spins complete a full 2π rotation for $B_{\parallel} < B_{cr}$ in both bands, but do not complete a full rotation for $B_{\parallel} > B_{cr}$.

bands, and the associated Berry phases of the spin-polarized eigenstates (given in Eq. (S4)) are $\gamma_p^{\pm} = \pm\pi$, such that $\gamma_p^+ + \gamma_p^- = 0$.

It is important to note that while the Berry curvature affects the semi-classical equations of motion, its contribution to the longitudinal second-harmonic current vanishes, as shown in Ref. [2]. Nevertheless, the sharp jump of the second-harmonic resistance occurs just as the Dirac point moves out of both Fermi contours, as demonstrated in Figure 5 of the main text. Beyond the critical field, $B_{\parallel} > B_{cr}$, the spins of the eigenstates do not complete a full rotation going around the Fermi contours. Furthermore, the out-of-plane magnetic field B_z opens a gap at the Dirac point, leading to a non-zero $J^{(2)}$ for $B_{\parallel} < B_{cr}$. In light of these observations, it is an interesting question whether our results could be related to topological properties of the energy bands.

E. Scattering time approximation, temperature, and gate-voltage

In our calculations, we assumed a single relaxation time τ . Furthermore, we assumed that the second-order current is characterized by τ^2 , leading to γ being independent of τ . As can be seen in the above calculations, and as demonstrated by Ideue *et al.* [1], even within this approximation, γ should change with temperature and carrier density. However, in our system, the dependence of γ on these parameters is too strong for the relatively small variations of temperature and gate-voltage (even when accounting for both the change in μ and in λ caused by the gate). A similar strong dependence of γ on temperature was previously observed in SrTiO₃ [3]. In that work, He *et al.* speculated that the assumption that the spin states are well-defined may be inaccurate and that coherent superpositions of spin states could substantially change the calculations. We also observe a strong dependence on gate-voltage, and note that as shown previously for the (111) LaAlO₃/SrTiO₃ interface [4], the spin-relaxation becomes dominated by a D’yakonov-Perel’ type mechanism at negative gates, resulting in incoherent spin-orbit scattering effects on transport. While it would be interesting to incorporate such effects into the calculations, such an analysis is beyond the scope of this work. We do however note that for a given temperature and gate-voltage, our minimal model is sufficient to explain the critical in-plane magnetic field, and the strong effect of the out-of-plane field.

II. SUPPLEMENTARY SECTION 2 — SAMPLE PREPARATION, EXPERIMENTAL METHODS:

22 mono-layers of LaTiO₃ were grown with the use of the Pulsed Laser Deposition (PLD) technique at a partial pressure of oxygen of 1×10^{-4} Torr, a temperature of 780 ° C, and energy density of $1.15 \frac{1}{\text{cm}^2}$. The layers were deposited on atomically flat, 0.5 mm thick (111) SrTiO₃ substrates. After deposition, the samples were annealed at 400 ° C and a pressure of 200 mTorr for 1 hour. The sample was then cooled to room temperature, and while still in the growth chamber, an 8.5 nm thick amorphous BaTiO₃ capping layer was deposited to prevent oxidation of LaTiO₃ to LaTiO_{3+δ}. This capping layer was grown at a partial pressure of oxygen of 1.5×10^{-3} Torr. The first 60 pulses were grown at a rate of 1 Hz, while the rest was grown at 3 Hz. The lithography-defined current paths along different crystallographic axes were defined with the use of an amorphous material hard mask (see Ref. [5] for details).

Back-gate electrodes were attached to the bottom of the SrTiO₃ substrates with Ag paint. Angle-dependence magneto-transport measurements were conducted using a two-axis piezo rotator in an Attocube attoDRY2100 system

with a maximal magnetic field of 9 T. Hall measurements up to 14 T were conducted in a Quantum Design Physical Property Measurement System (PPMS). Superconductivity measurements were conducted in a Oxford Instruments Triton dilution refrigerator with a base temperature of 20 mK and a (8 T, 1 T, 1 T) vector magnet. Measurements throughout this work were conducted in different instruments and cool-downs, resulting in slight variations of sheet resistances and base temperatures in different measurements. Second-harmonic transport measurements were conducted by driving an alternating current with an amplitude of 100 μA using a Keithley 6221 current source. A trigger link was connected from the current source to a Stanford Research Systems SR830 lock-in, set to measure the second harmonic with a $-\frac{\pi}{2}$ phase. To account for the slight out-of-plane wobble of the sample while rotating the in-plane angle ϕ , the out-of-plane angle θ changed along with ϕ to remain perfectly in-plane. The exact θ corresponding to the in-plane orientation was calibrated for several ϕ angles prior to the measurement by measuring the sharp in-plane peak seen in the second-harmonic transport (as seen in Fig. 3(a)).

III. SUPPLEMENTARY SECTION 3 — ADDITIONAL MEASUREMENTS:

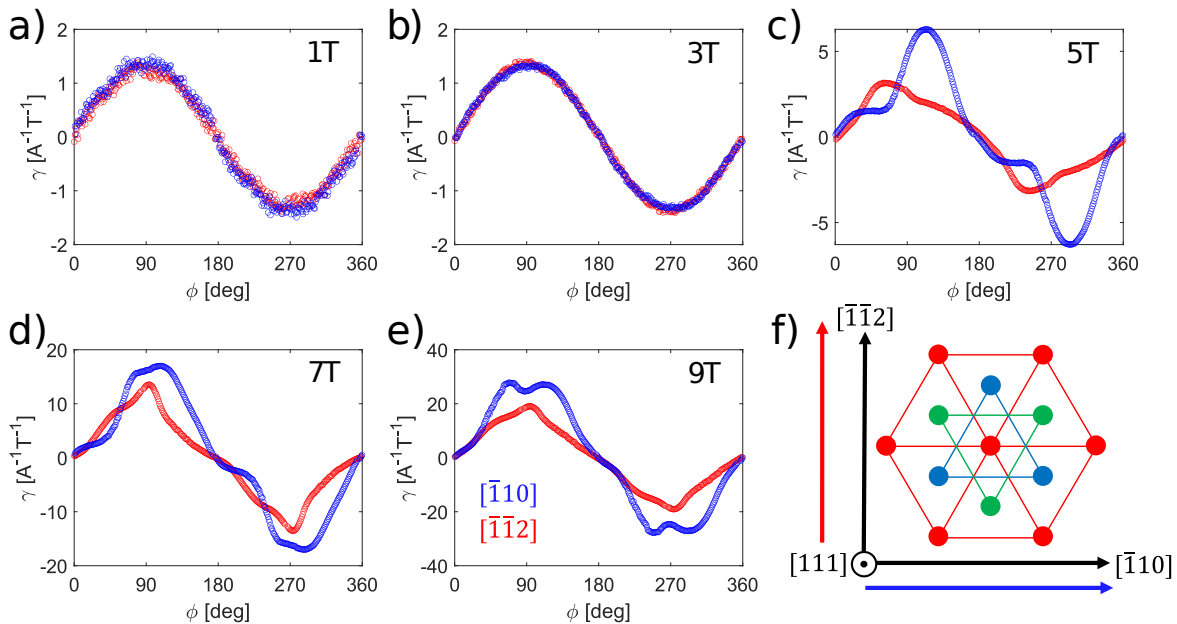


FIG. S2. Non-linear transport coefficient γ versus ϕ for two Hall bar devices patterned along different crystal axes subjected to various in-plane magnetic fields. Data in blue/red corresponds to devices with current running along the $[\bar{1}\bar{1}0]/[\bar{1}\bar{1}2]$ axis. ϕ is defined as the angle between the current and the magnetic field. (a)-(e) Shows data for various magnitudes of the magnetic field from 1 T to 9 T. (f) Sketch of the $[111]$ face of the Ti atoms in the SrTiO_3 crystal. Different colors of the atoms correspond to different locations along the $[111]$ axis. Blue/red arrows mark the direction of current for the data shown here. Data shown in blue ($I \parallel [\bar{1}\bar{1}0]$) corresponds to the device shown in the main text. Measured at $T=3$ K and $R_s=380$ Ω for the $[\bar{1}\bar{1}0]$ device, and $R_s=404$ Ω for the $[\bar{1}\bar{1}2]$ device.

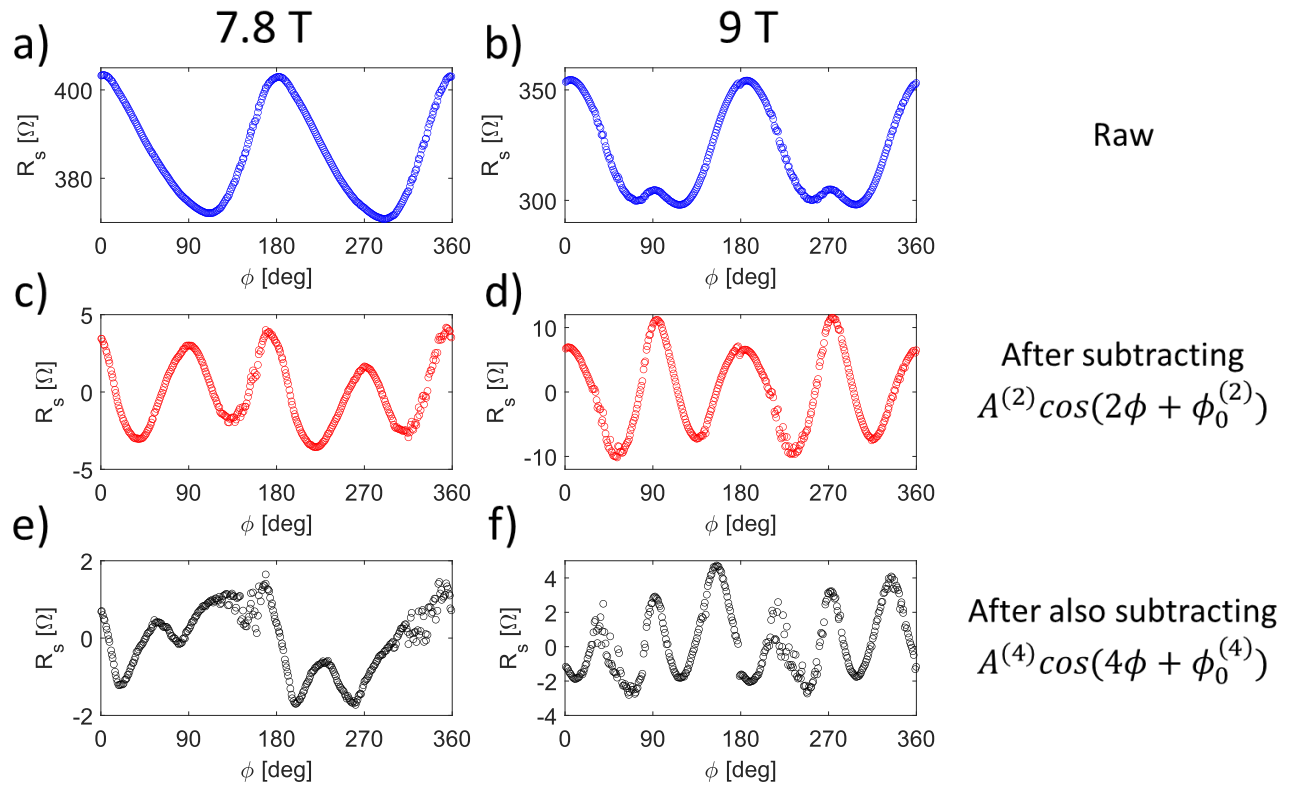


FIG. S3. In-plane first-harmonic magnetoresistance measurements for the device shown in the main text. (a)-(b) Raw data of resistance versus in-plane magnetic field angle for magnetic field magnitudes of 7.8 T and 9 T. A mostly two-fold dependence on ϕ is observed. (c)-(d) Data after subtracting two-fold component (via Fourier), revealing a mostly four-fold behavior. (e)-(f) After also subtracting the four-fold component, a six-fold behavior can be seen. The effect is larger and hence can be observed more clearly at 9 T. Data taken from device shown in main text. 9 T measurement set conducted at $T=3$ K and $R_s=380$ Ω , 7.8 T measurements at $T=2$ K and $R_s=407$ Ω

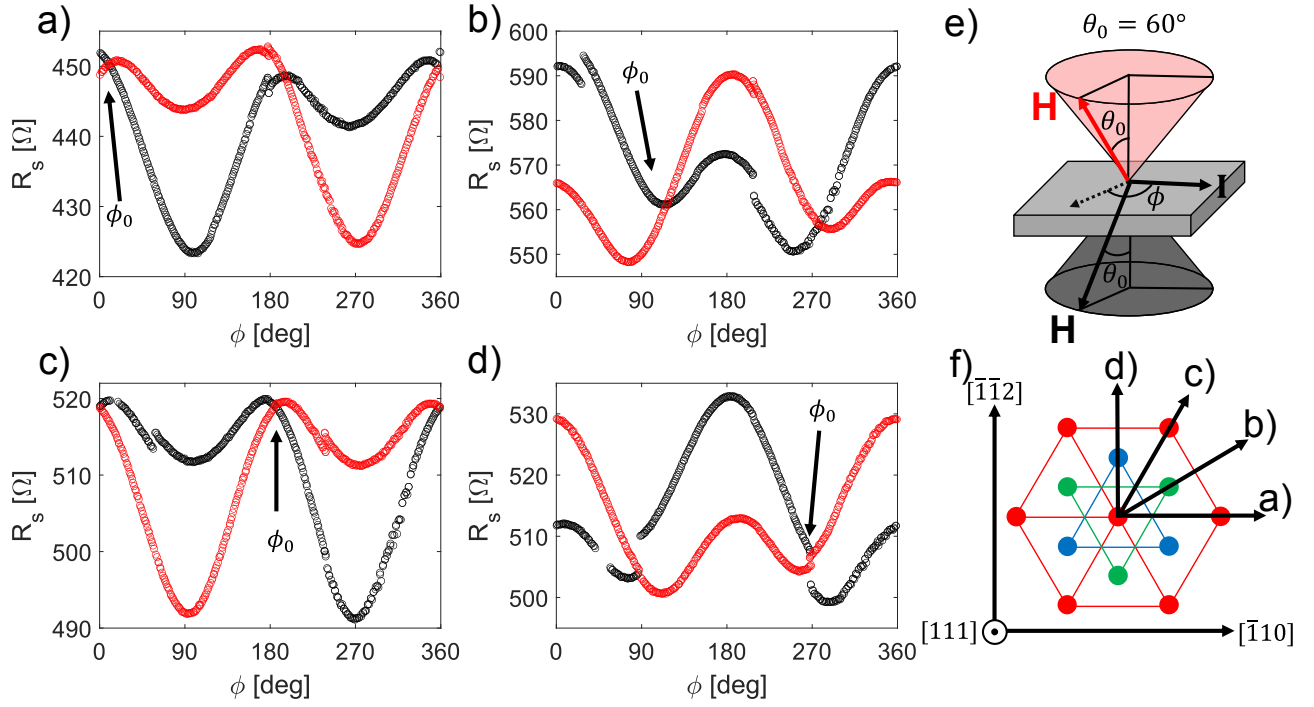


FIG. S4. Resistance versus in-plane magnetic field angle ϕ while keeping a constant positive/negative out-of-plane magnetic field is shown in red/black. (a)-(d) Measurements are shown for four different devices where current is driven along different crystal axes. (e) Sketch of magnetic field orientation. (f) Sketch of the [111] face of the crystal, showing the direction of current in (a)-(d). The angle ϕ_0 , defined as the angle where both curves intersect (see also main text), rotates by 90° whenever the current is rotated by 30° , reflecting the three-fold symmetry of the [111] face. In-plane magnetic field is always 7.8 T, while out-of-plane field is 4.5 T (red) and -4.5 T (black). $T=1.9$ K, and R_s for various devices are: (a) 474 Ω , (b) 608 Ω , (c) 541 Ω , (d) 531 Ω . Resistances here vary more significantly from rest of figures since no gate-voltage was applied.

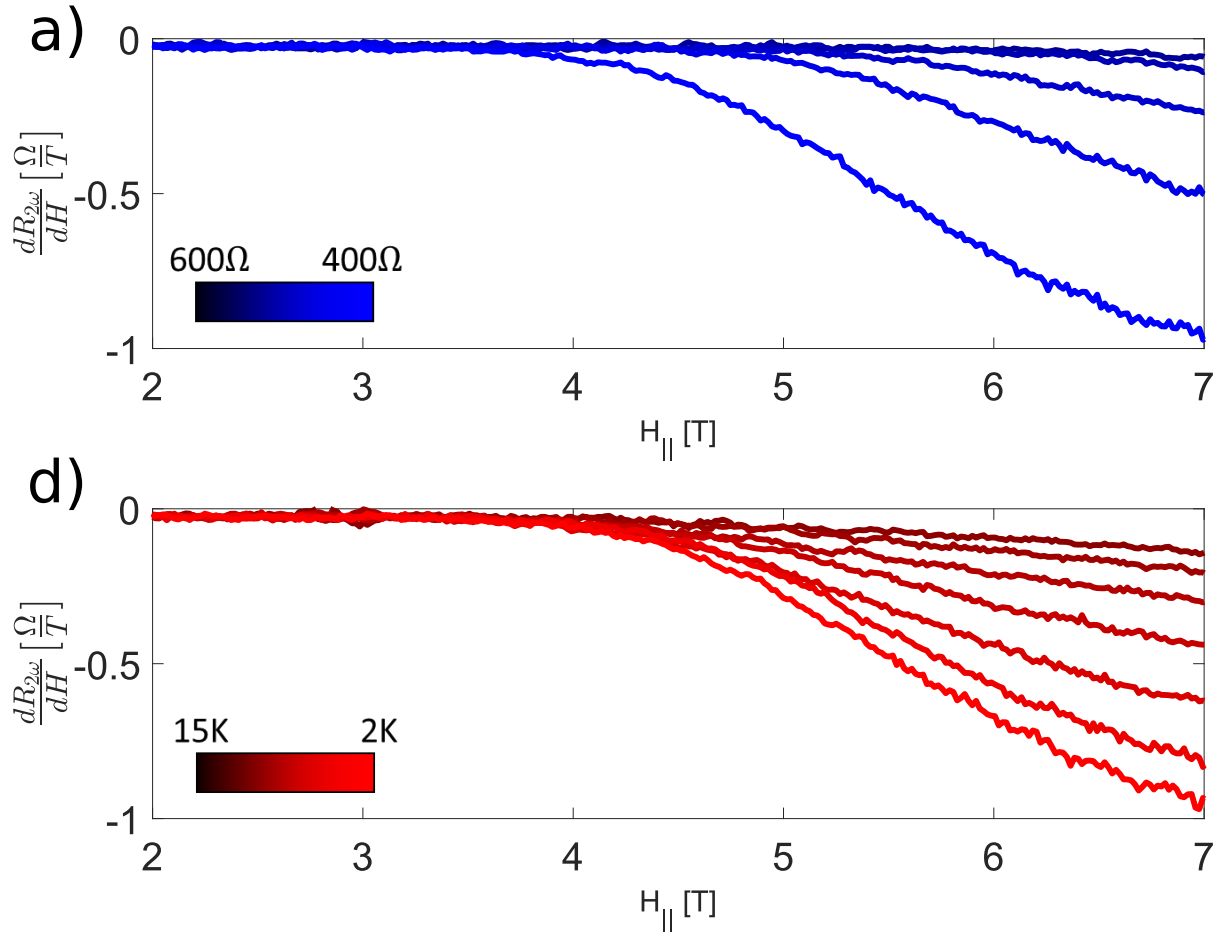


FIG. S5. Derivative of $R_{2\omega}$ with respect to the magnetic field for various gates (a) and temperatures (b). Data corresponds to measurement shown in main text. By examining the derivative, a clear change in the critical magnetic field can be observed for different gates, while temperature mostly reduces the magnitude of the effect but does not change H_{cr} .

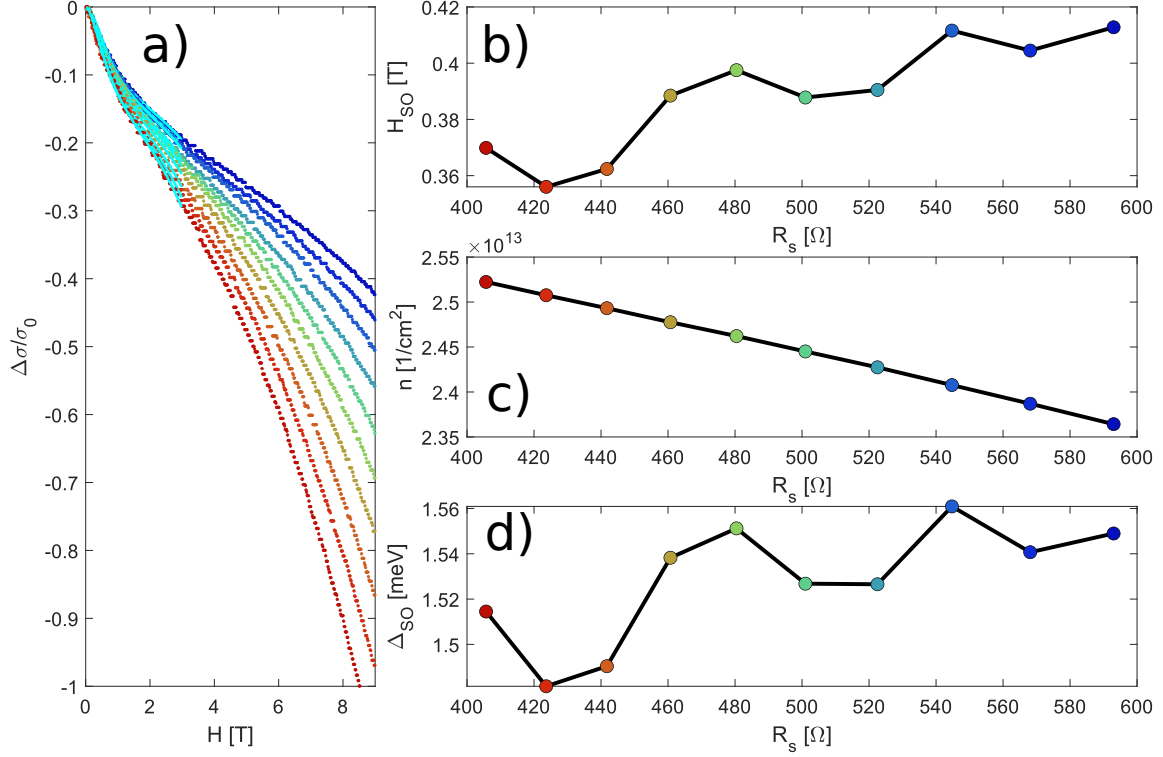


FIG. S6. (a) Weak anti-localization measurements presented as change in conductivity divided by the quantum conductance as function of perpendicular magnetic field. Cyan lines correspond Hikami-Larkin-Nagaoka fit for diffusive two-dimensional electrons with negligible Zeeman splitting (see Lesne *et al.* for similar analysis [6]). Different colors correspond to different gate voltages. (b) Spin-orbit field H_{SO} extracted from the fits shown in (a) for various gate-voltages (see x-axis for corresponding sheet resistance of every measurement). (c) Two-dimensional electron density extracted from Hall measurements. (d) Spin-orbit energy Δ_{SO} calculated using (b), (c), and taking an effective mass of $3m_e$. Measurements conducted at 2 K. The contribution of the Hall resistance to σ was neglected.

IV. SUPPLEMENTARY SECTION 4 — EFFECT OF IN-PLANE MAGNETIC FIELD ON THE HALL EFFECT:

The Hall effect shown in the main text only contains a perpendicular magnetic field and shows a perfect linear behavior. However, a planar magnetic field was previously shown to contribute to the Hall signal in two distinct ways in the $\text{LaAlO}_3/\text{SrTiO}_3$ interface. In this section we demonstrate that these effects are also observed in the (111) $\text{LaTiO}_3/\text{SrTiO}_3$ interface studied here.

In Figure S7 we show the anomalous planar Hall effect for various gate-voltages. This is a Hall contribution appearing even when the magnetic field is completely in the plane of the interface. A linear low-field slope can be observed followed by an anomalous contribution beyond some critical in-plane field. As the gate-voltage becomes more negative (higher resistance), the anomalous planar behavior is not observed. Similar effects were recently observed in the (111) $\text{LaAlO}_3/\text{SrTiO}_3$ interface and related to the formation of Berry curvature dipoles [6]. In that system, this behavior was reported only once a two-band behavior was observed in the normal Hall signal. However, in the interface studied here, this planar Hall effect appears despite the presence of only one electronic band. It is important to note that results were antisymmetrized with respect to the magnetic field to prevent contributions from the symmetric planar Hall effect which originates from anisotropic magnetoresistance.

We also note that we can confirm that the low-field linear slope is real and is not a result of a misalignment artifact. We are able to confidently make this claim since these measurements were conducted in a dilution refrigerator with a vector magnet. Prior to the planar Hall measurements, the sample was brought exactly to its superconducting critical temperature (defined as half the normal-state resistance) under the presence of a 1 T in-plane magnetic field. Then, a small out-of-plane magnetic field was applied and varied slowly. We show the results of longitudinal resistance in the inset of Figure S7 where a clear minimum of resistance can be seen. Since the superconductivity is much more

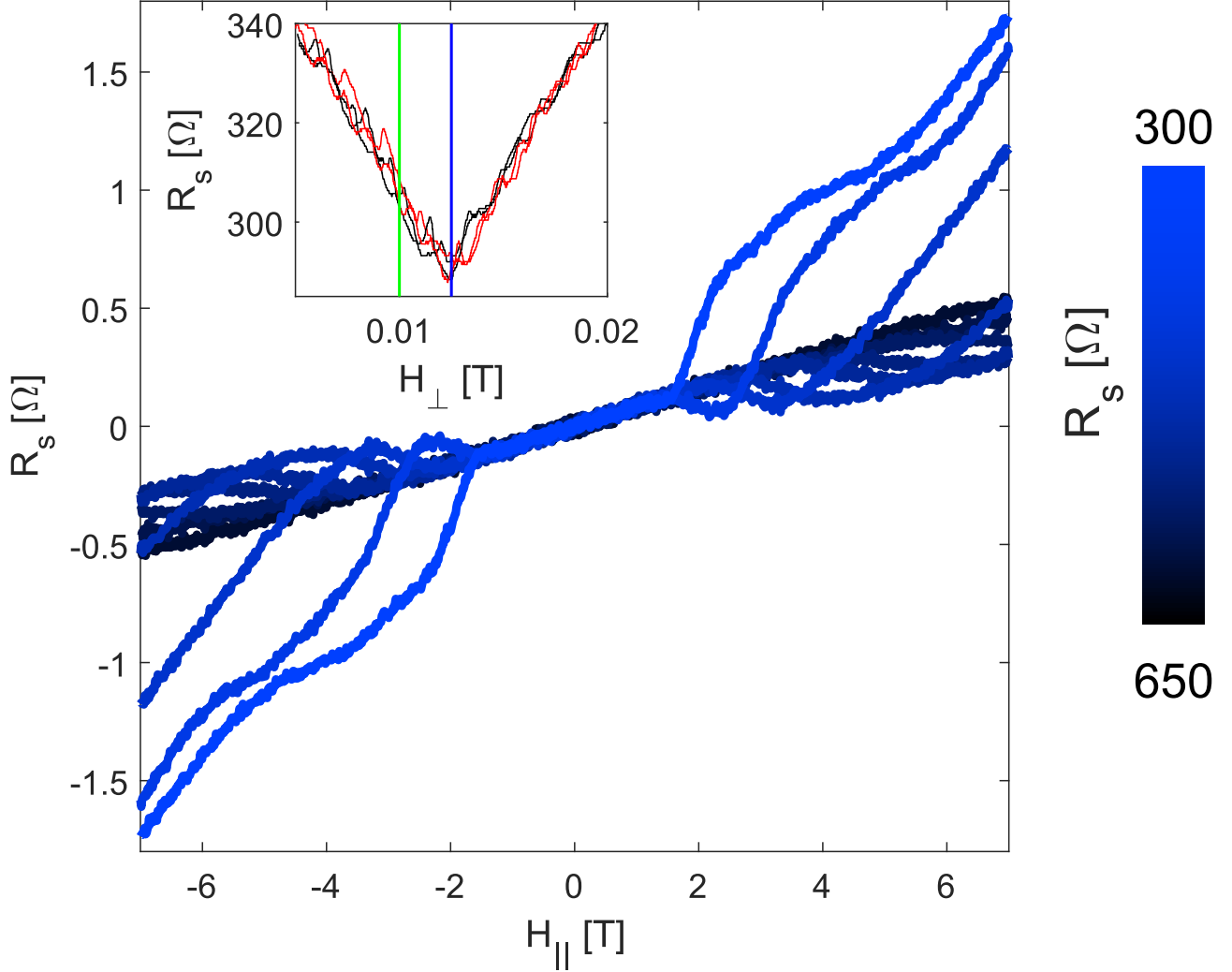


FIG. S7. Anomalous planar Hall effect. We show the results of the the antisymmetric Hall effect at $T=0.7$ K when the magnetic field is completely in the plane of the interface. A linear slope is seen followed by an anomalous planar contribution. Inset: Alignment measurements explained in the text of this section.

sensitive to an out-of-plane magnetic field, the system will be closest to the superconducting state (lower resistance) when the magnetic field is exactly in the plane of the interface. Therefore, we can use this measurement to accurately account for the misalignment of our sample and the measurements shown here and in the following figure are corrected for this misalignment. To further illustrate this point, we mark in the inset the amount of misalignment field needed to explain the linear slope from a normal Hall effect contribution through misalignment (green line). As can be seen, our accuracy is much better than this amount of misalignment. This alignment measurement was repeated four times with varying sweep directions (black/red) to account for thermal fluctuations.

When both in-plane and out-of-plane magnetic fields are applied, a different contribution to the Hall effect is measured. We show this in Figure S8 (a), where a constant magnetic field of 7 T is applied in the plane of the interface and an out-of-plane magnetic field is changed. It can be seen that for more negative gate voltages (high R_s), the Hall effect is linear with the out-of-plane field, meaning the it is unaffected by the presence of the in-plane field. However, for more positive gate voltages, an anomalous contribution to the Hall effect can be observed. This anomalous Hall effect was previously observed in the $\text{LaAlO}_3/\text{SrTiO}_3$ interface [7, 8]. As noted in the main text, these effects were only observed along with a two-band Hall effect, while in our interface they appear with a single occupied band.

In Figure S8 (b), we apply a constant out-of-plane field while changing the in-plane magnetic field. We then plot the measured Hall resistance after subtracting the Hall resistance for zero-in-plane magnetic field. The resulting resistance

is the anomalous contribution to the Hall effect from the in-plane magnetic field. In the inset of this figure, we show the anomalous contribution for $H_{\parallel}=7$ T, $H_{\perp}=0.3$ T versus the sheet-resistance (gate-voltage). It can be seen that the anomalous contribution decays when the sheet resistance is larger (more negative gate-voltage). The appearance of these effects only when a large in-plane magnetic field and a positive gate-voltage are applied leads us to speculate that they are also related to the exclusion of the Dirac point from the Fermi surface and the related change to the Fermi surface and spin texture.

We note that these measurements were antisymmetrized with respect to the total field,

$$R_{xy}(H_{\parallel}, H_{\perp}) = \frac{R_{xy}(H_{\parallel}, H_{\perp}) - R_{xy}(-H_{\parallel}, -H_{\perp})}{2}. \quad (\text{S17})$$

The Hall resistance was then antisymmetrized again with respect to H_{\perp} to remove the contribution of the anomalous planar Hall effect shown in Figure S7.

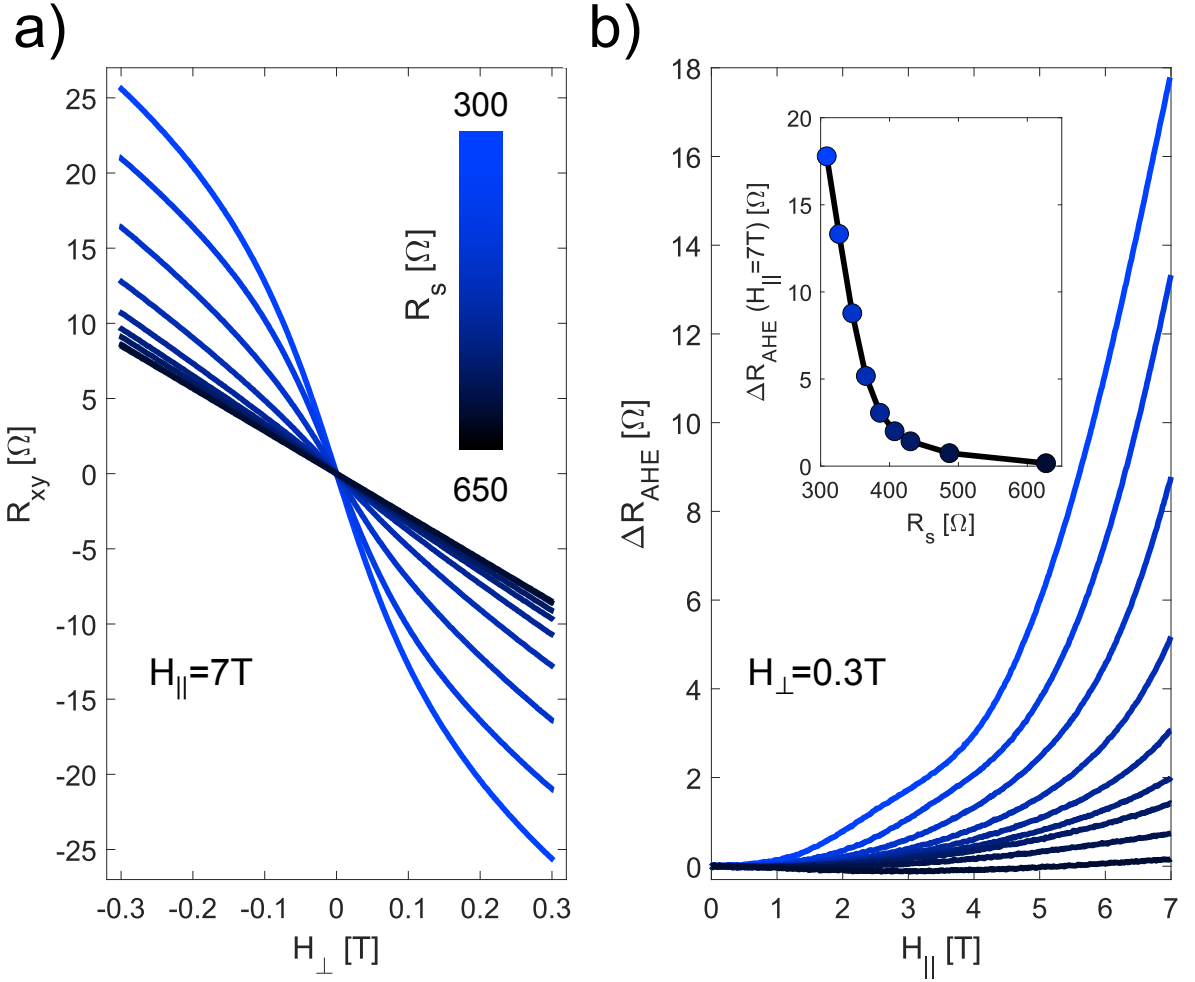


FIG. S8. Constant in-plane magnetic field drives anomalous Hall behavior. (a) A constant in-plane magnetic field of 7 T is kept while the out of plane magnetic field is swept shown for various gate voltages. To remove contributions of the planar Hall effect, each magnetic field sweep is repeated with -7 T and the data is antisymmetrized with respect to the total magnetic field. To remove contributions from the anomalous planar Hall effect (which is antisymmetric with the in-plane field, see previous figure) the results are antisymmetrized again with respect to the perpendicular magnetic field. As the gate-voltage becomes more positive (lower resistance), the anomalous contribution to the Hall effect increases. (b) Similar to the analysis done in (a), but the out-of-plane magnetic field was constant at 0.3 T, while the in-plane magnetic field was swept. The normal Hall resistance (no in-plane field) was subtracted from all the measurements to show the anomalous component. Inset: anomalous contribution for $H_{\parallel}=7$ T, $H_{\perp}=0.3$ T versus the sheet-resistance (gate-voltage). All measurements conducted at $T=0.7$ K.

-
- [1] T. Ideue, K. Hamamoto, S. Koshikawa, M. Ezawa, S. Shimizu, Y. Kaneko, Y. Tokura, N. Nagaosa, and Y. Iwasa, [Nature Physics](#) **13**, 578 (2017).
 - [2] R. Battilomo, N. Scopigno, and C. Ortix, [Phys. Rev. Res.](#) **3**, L012006 (2021).
 - [3] P. He, S. M. Walker, S. S.-L. Zhang, F. Y. Bruno, M. S. Bahramy, J. M. Lee, R. Ramaswamy, K. Cai, O. Heinonen, G. Vignale, F. Baumberger, and H. Yang, [Phys. Rev. Lett.](#) **120**, 266802 (2018).
 - [4] P. K. Rout, E. Maniv, and Y. Dagan, [Phys. Rev. Lett.](#) **119**, 237002 (2017).
 - [5] E. Maniv, M. B. Shalom, A. Ron, M. Mograbi, A. Palevski, M. Goldstein, and Y. Dagan, [Nature Communications](#) **6**, 8239 (2015).
 - [6] E. Lesne, Y. G. Sağlam, R. Battilomo, M. T. Mercaldo, T. C. van Thiel, U. Filippozzi, C. Noce, M. Cuoco, G. A. Steele, C. Ortix, and A. D. Caviglia, [Nature Materials](#) **22**, 576 (2023).
 - [7] M. Ben Shalom, M. Sachs, D. Rakhmilevitch, A. Palevski, and Y. Dagan, [Phys. Rev. Lett.](#) **104**, 126802 (2010).
 - [8] A. Joshua, J. Ruhman, S. Pecker, E. Altman, and S. Ilani, [Proceedings of the National Academy of Sciences](#) **110**, 9633 (2013).